



Design and characterization of color printed polyurethane films as biomedical phantom layers

CLAUDIA F. MORSINK,^{1,†} ALIDA J. DAM-VERVLOET,^{1,2,†} MARLEEN E. KROMMENDIJK,¹  MICHAEL KAYA,¹ CARLOS CUARTAS-VÉLEZ,¹ TOM KNOP,¹  KALLOOR JOSEPH FRANCIS,^{1,‡,*}  AND NIENKE BOSSCHAART^{1,3,‡}

¹Biomedical Photonic Imaging Group, Technical Medical Center, University of Twente, The Netherlands

²Medical Physics Department, Isala Hospital, Zwolle, The Netherlands

³n.bosschaart@utwente.nl

[†]These authors contributed equally to this work.

[‡]These authors contributed equally to this work and should be considered co-senior authors.

*f.kalloorjoseph@utwente.nl

Abstract: We propose a new, user-friendly and accessible approach for fabricating thin phantoms with controllable absorption properties in magnitude, spectral shape, and spatial distribution. We utilize a standard office laser color printer to print on polyurethane thin films (40 – 60 μm), commonly available as medical film dressings and ultrasound probe covers. We demonstrate that the optical attenuation and absorption of the printed films correlate linearly with the printer input settings (opacity), which facilitates a systematic phantom design. The optical and acoustic properties of these polyurethane films are similar to biological tissue. We argue that these thin phantoms are applicable to a wide range of biomedical applications. Here, we introduce two potential applications: (1) homogeneous epidermal melanin phantoms and (2) spatially resolved absorbers for photoacoustic imaging. We characterize the thin phantoms in terms of optical properties, thickness, microscopic structure, and reproducibility of the printing process.

© 2023 Optica Publishing Group under the terms of the [Optica Open Access Publishing Agreement](#)

1. Introduction

Phantoms are indispensable in the development, validation, optimization, and quality control of any new technique in biomedical optics. An adequate phantom has known optical properties that can be controlled with high accuracy while mimicking the optical properties of tissue in the desired wavelength range. In the case of photoacoustic phantoms, not only the optical but also the acoustic properties should match those of biological tissue. Many phantom fabrication approaches are available in biomedical optics, based on either liquid or solid phantom matrix materials (e.g. water, hydrogel, silicone, polymer, and gel-based), a wide variety of light scatterers (e.g. lipid droplets, microspheres, powders) and different types of light absorbers (e.g. dyes, printer toner, black silicone) [1–6]. Some of the phantom fabrication approaches involve highly complex geometries and functions [7–12].

Although highly advanced approaches for phantom fabrication are effective, not all biomedical optics laboratories have the necessary resources and equipment to produce these phantoms. In particular thin phantom layers (<100 μm) with controllable optical properties are difficult to fabricate without advanced equipment such as spin coating, lithography, and 3D-printing [8,13–17]. These thin phantom layers are of particular interest to mimic the thin tissue layers, for example, epithelial tissue and vascular structures.

We propose a new approach to fabricate thin phantom layers with controllable absorption properties in magnitude, spectral shape, and spatial distribution. Compared to the available

methods for thin phantom layer fabrication, our proposed method is easy to implement in any lab environment as it utilizes a standard office laser printer to print four toner colors (yellow, magenta, cyan, and black) on thin, polyurethane films. These polyurethane films are commonly available as medical film dressings (thickness $\sim 40\ \mu\text{m}$) and ultrasound probe protection covers (thickness $\sim 60\ \mu\text{m}$). To further enhance the usability of this approach, we introduce and test a method to directly relate the printer input settings (opacity) to the optical properties of the printed film. We demonstrate two potential applications for these thin phantom layers: 1) homogeneous epidermal melanin phantoms and 2) spatially resolved absorbers as phantoms for photoacoustic imaging. Printing phantoms for testing imaging systems is not entirely new, it has been previously demonstrated in X-ray imaging [18–20] and in photoacoustic imaging [16,21]. In our work, we aim to advance this approach by optimal material selection in terms of both optical and acoustic properties, establishing a reproducible printing procedure, using all toner colors instead of a single (mostly black) toner, and demonstrating control over the optical properties of the printed phantoms.

The relevance of the first application relates to the necessity of having reliable epidermal melanin phantoms for characterizing the influence of skin color on optical device performance. Many optical techniques unintentionally suffer from a readout bias towards darker skin tones [22–25]. The epidermal melanin phantoms in this paper have been optimized for transcutaneous bilirubin measurements on newborn skin, which has an average epidermal thickness of $43\ \mu\text{m}$ [26]. The absorption properties of the epidermal melanin phantom are optimized for the wavelengths 450 nm and 550 nm, which are commonly used in many commercial bilirubin meters.

The second application builds upon one of the current challenges in photoacoustic imaging. There already exists a significant body of research on phantom development in photoacoustic imaging [7–12]. Developing complex vascular phantoms with accurate ground truth information using current solid phantom technologies remains a challenging task. While the current techniques make it feasible to create test phantoms with simple geometric inclusions, achieving precise ground truth structural information is difficult [2]. Deviation from the ground truth structural information is common due to the chemical fabrication process, which often involves heating, cooling, and the use of molds for casting. An alternative approach is to manufacture a phantom and obtain the ground truth information by imaging it using CT or MRI [27]. Printing vascular structures was previously tested in photoacoustic imaging [16,21], especially in the context of tomographic imaging systems. In this work, our objective is to build upon the existing approach by focusing on appropriate material selection for printing and developing a method for photoacoustic imaging using a linear transducer array. By employing the proposed phantom printing approach, we can create phantoms with complex vascular structures that possess both ground truth information and controllable optical absorption. The significance of this method lies in its potential to facilitate the testing of image reconstruction algorithms and quantitative imaging techniques.

In this study, we characterize the geometrical and optical properties of the polyurethane films and the printed toner colors using collimated transmission, optical coherence tomography, white light microscopy, and photoacoustic imaging. Based on the absorption spectra of the pure toner colors, we develop a model to predict the absorption spectrum of the printed films for any printer input. This model is employed for the application of the epidermal melanin phantoms. The possibilities for printing spatially resolved absorbers are evaluated for the photoacoustic phantoms and tested for imaging accuracy using a handheld probe.

2. Methods

In this section, we present a detailed description of thin film phantom preparation, the employed printing procedure and the characterization of the printed phantoms. We then present how to use

the method for two applications, mimicking the epidermal melanin layer, and in photoacoustic imaging.

2.1. Phantom layers

2.1.1. Material selection

Polyurethane is selected as the printing material because the thermal, optical, and acoustic properties are well suited for this application. The melting temperature of polyurethane is 180°C, which can withstand the fuser temperature of the printer used in this study (175°C for the Xerox 7800i series printer). The optical absorption of polyurethane is 0.001 – 0.005 mm⁻¹ in the visible and near-infrared (NIR) wavelengths, which minimizes background absorption [28]. The refractive index of polyurethane is 1.41 – 1.58, which is within the range of the refractive index of soft tissue (1.35 – 1.55) [29,30]. Polyurethane polymer has a reported linear frequency-dependent attenuation coefficient of 4 dB cm⁻¹ MHz⁻¹ in the 1–10 MHz range and close acoustical impedance (1.7×10^6 Pa s m⁻¹) to that of biological tissues [31]. Based on the composition, polyurethane has been shown to be tunable to the acoustic attenuation coefficient of soft tissue 0.1–1.6 dB cm⁻¹ MHz⁻¹ [31,32]. Further, literature shows a range of speed of sound for polyurethane based on the composition from 1395 to 1615 m s⁻¹ [33,34], with a typical value of 1497 m s⁻¹ [35]. The speed of sound is within the range 1450 – 1730 m s⁻¹ for tissue [32]. Another important advantage of polyurethane is that it is a widely used material in medical applications and it is commonly available in thin film applications, for example in dressing and ultrasound transducer protection covers.

We used two commercially available polyurethane films in this work: (i) Tegaderm transparent adhesive dressing film (3M, Delft, The Netherlands) with a thickness of ~ 40 μm and (ii) ultrasound protection cover (PCU Protection Cover Ultrasound B.V, The Netherlands) of thickness ~ 60 μm. The films were selected based on the target application. Tegaderm was selected as a substrate for mimicking the epidermal melanin layer, because the film must be flexible and attachable to the skin, to the optical device, or to other phantom materials that e.g. mimic the dermis. To create photoacoustic phantoms, the adhesivity of the film is not necessary, but the film should be non-stretchable to ensure that the printed phantom matches the digital image. To meet this requirement, we selected an ultrasound transducer protection cover (US cover) for this application.

2.1.2. Printing procedure

Figure 1(A) presents a schematic overview of the printing procedure. The printer used in this study is a standard office laser printer (Xerox 7800 series, type WorkCentre 7835i). This printer utilizes four toner colors, namely cyan (C), magenta (M), yellow (Y), and black (K), with corresponding Xerox WW metered codes of 006R01512, 006R01511, 006R01510, and 006R01509.

Proper alignment of the polyurethane film for printing was achieved by printing a guide square with the desired size on A4 paper. The transparent polyurethane film (35 × 35 mm² for epidermal melanin phantoms and 120 × 60 mm² for photoacoustic phantoms) was positioned over this square and fixed with tape (Scotch Magic tape) on the edges of the film, avoiding the printing area. Next, the paper with the polyurethane film was printed again, thus assigning the desired printer input to the location of the guide square where the film was attached. After printing, the tape was removed without causing any damage to the polyurethane films. Please note that no stacking of polyurethane films is applied in this study. All phantoms consist of a single polyurethane film, only the print opacity was varied between films.

For this study, the input settings for printing and communication with the printer were achieved through the open-source graphics software Inkscape (version 1.2). These input settings consist of two variables that together define the print color and opacity: the color opacity for each

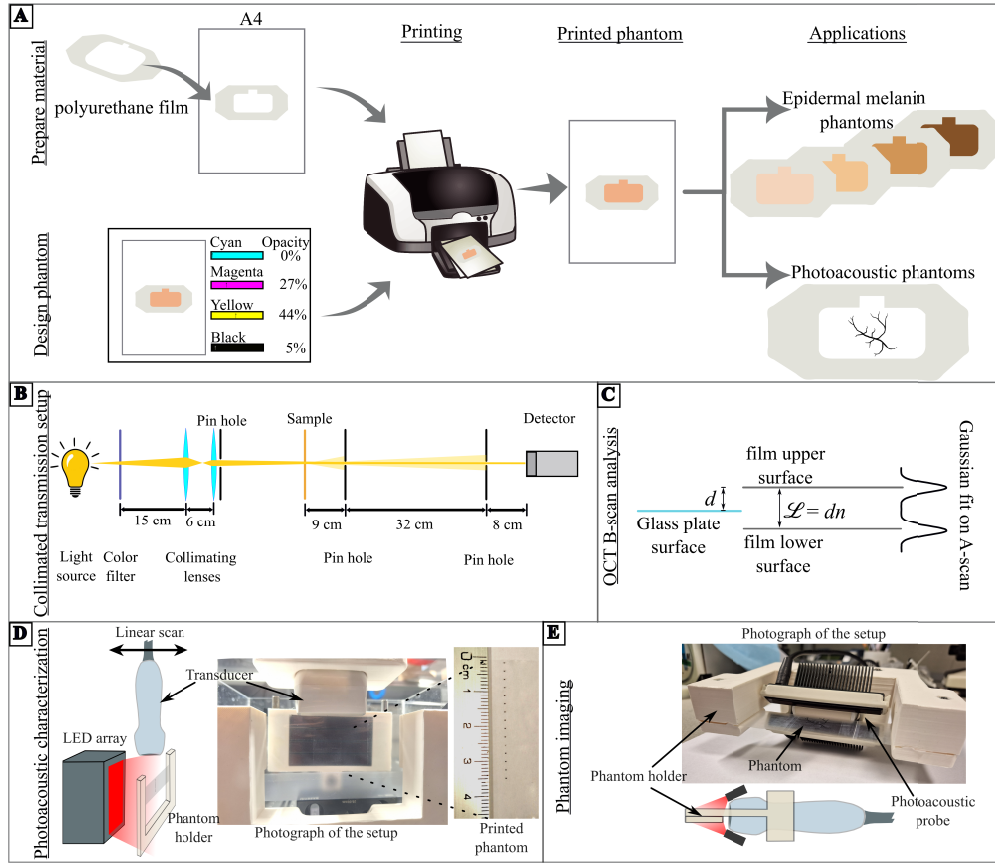


Fig. 1. Phantom development procedure and optical characterization. (A) (Left) Phantom preparation using printing technology by selecting the desired opacity levels of toner to control the optical properties. (Right) Two target applications for a series of melanin phantoms and a vascular phantom. Please note that no stacking of polyurethane films is applied. All phantoms consist of single polyurethane films. (B) Collimated transmission setup to measure the optical properties of the printed phantoms. (C) Schematic illustration of the OCT B-scan analysis of a polyurethane film on a glass plate. The film has an actual thickness of d and an optical thickness of $\mathcal{L} = dn$, with n the refractive index of the film material. (D) A use case of the phantom in photoacoustic imaging, demonstrating the measurement of the elevational field of view of a transducer with a printed phantom oriented vertically to the transducer. (E) Imaging complex photoacoustic phantoms, where a phantom holder is employed to align the phantom with the imaging plane.

individual toner color O_j (with $j = C, M, Y, K$) and the print opacity O_P (ranging from 0% = no ink to 100% = full ink coverage). As the print opacity O_P scales the overall opacity of the print, the total printed opacity per color $O_{T,j}$ will be scaled down with respect to O_j if more colors are included in the print. For example, if the color opacity O_j is set at 100% for two colors (e.g. $O_C = 100\%$, $O_M = 100\%$, $O_Y = 0\%$ and $O_K = 0\%$) and the print opacity is set at $O_P = 100\%$, then the total printed opacity will be 50% for cyan and 50% for magenta. Thus, the total printed opacity per color $O_{T,j}$ is defined as

$$O_{T,j} = \frac{O_j O_P}{J \times 100\%}, \quad (1)$$

where J is the total number of colors that will be printed. If multiple toner layers l are printed on top of each other by printing a single film multiple times, this will further increase the total printed opacity to

$$O_{T,j} = \sum_{l=1}^L O_{T,j,l}, \quad (2)$$

with L being the total number of printed toner layers on top of a single polyurethane film and $O_{T,j,l}$ the total printed opacity per color per toner layer. Please note that the concept 'layer' here should not be confused with the digital namesake used to identify multiple objects or layers in Inkscape and other graphics software. In case the print settings $O_{j,l}$ and $O_{P,l}$ are identical for each printed toner layer and the print opacity $O_{P,l}$ is always set at 100%, we can simplify Eq. (2) to

$$O_{T,j} = \frac{L}{J} O_{j,l}. \quad (3)$$

To facilitate phantom design, ideally, the optimal print settings for a desired absorption coefficient spectrum $\mu_a(\lambda)$ as a function of the wavelength λ should be defined. This is possible if the absorption coefficient spectra $\mu_{a,j}(\lambda)$ of the pure toner colors at an opacity $O_P = 100\%$ are known. In that case, $\mu_a(\lambda)$ can be defined as

$$\mu_a(\lambda) = \sum_j \mu_{a,j}(\lambda) O_{T,j}. \quad (4)$$

The optimal print settings $O_{T,j}$ can be derived from Eq. (4) if the desired $\mu_a(\lambda)$ is defined within the wavelength range of the known $\mu_{a,j}(\lambda)$ of the pure toner colors. In Section 2.1.4 we give an example of how these optimal print settings can be derived for the application of epidermal melanin phantoms.

2.1.3. Printed films: pure toner colors

For all pure toner colors (C , M , Y , and K), we generated a series of printed Tegaderm films with opacities ($O_{T,j}$) that ranged between 25% and 175%. An overview of these samples and the corresponding printer input settings are provided in Table 1. Three Tegaderm films were printed with identical printer input settings for each $O_{T,j}$, in order to evaluate the reproducibility of the phantom fabrication process. The attenuation and absorption coefficient spectra were measured using a collimated transmission setup (Section 2.2.1), the thickness and refractive index were evaluated using optical coherence tomography (Section 2.2.2), and the microscopic structure was evaluated using white light microscopy (Section 2.2.3). The same measurements were performed on 15 unprinted films for both polyurethane film types (Table 1).

2.1.4. Application 1: homogeneous epidermal melanin phantoms

For the application described next, we develop a series of epidermal melanin phantoms that can be used to evaluate the influence of skin pigmentation on transcutaneous bilirubin measurements. Transcutaneous bilirubin meters are optical devices that estimate bilirubin concentrations in the skin of jaundiced newborns. Bilirubin concentrations are derived from the optical attenuation at two or more wavelengths and one or more optical path lengths, thereby aiming to correct the background absorption of hemoglobin and melanin [36]. Two of the most commonly used transcutaneous bilirubin meters in the clinic are the JM-103 and the JM-105 (Dräger Medical, Lübeck, Germany), which operate at 450 and 550 nm. The average thickness of the newborn epidermis ($\sim 43 \mu\text{m}$) is comparable to the thickness of the Tegaderm films used in this study ($\sim 40 \mu\text{m}$) [26].

Whereas we have focused on the development of dedicated dermal phantoms for transcutaneous bilirubin measurements in our previous work [36,37], these phantoms did not yet incorporate

Table 1. Overview of phantom series only with pure toner colors.

Film type	Printer input setting			Number of films
	$O_{T,j}$ (%)	$O_{j,l}$ (%)	L	
Unprinted films				
Tegaderm	-	-	-	15
Ultrasound cover	-	-	-	15
Tegaderm	25	25	1	3
pure colors	50	50	1	3
$(j = Y, M, C, K)$	60	60	1	3
	75	75	1	3
	90	90	1	3
	100	100	1	3
	125	100 ($l = 1$)	2	3
		25 ($l = 2$)	2	3
	150	100 ($l = 1$)	2	3
		50 ($l = 2$)	2	3
	175	100 ($l = 1$)	2	3
		75 ($l = 2$)	2	3
Ultrasound cover	30	30	1	3
pure colors	60	60	1	3
$(j = K)$	100	100	1	3

the epidermal attenuation by melanin. To develop a series of epidermal phantoms with varying melanin concentrations, we have to match the optical absorption of the printed films at two wavelengths (450 and 550 nm) with the known melanin absorption spectra from the literature. Literature values for the epidermal absorption are obtained from Jacques [30] for six different volume fractions of melanosomes f_{mel} , as presented in Table 2. This range of melanosome volume fractions corresponds to a range of light skin (1.3–6.3%) to moderately pigmented skin (11–16%), to darkly pigmented skin (18–32%) [38]. Whereas Jacques reports melanosome volume fractions up to 45% [38], we limit the range here to 32% because neonatal skin is significantly less pigmented than adult skin [39,40]. Exact values for melanosome volume fractions in neonatal skin have not been reported in the literature.

We obtain the optimal printer input settings for the desired absorption coefficients with Eq. (3) and (4) for two toner colors (yellow and magenta), at 450 and 550 nm. Hereto, the measured absorption spectra $\mu_{a,j}(\lambda)$ for the phantoms printed with pure toner colors are used (Table 1 and Fig. 3). A possible solution for the optimal printer settings is given in Table 2. For this solution, the maximum opacity for yellow is set at 60%, the color opacities per printed toner layer ($O_{Y,l}$ and $O_{M,l}$) remain constant, and only the number of printed toner layers L varied.

A series of epidermal melanin phantoms are printed using the input settings from Table 2. The attenuation and absorption coefficient spectra are measured using a collimated transmission setup (Section 2.2.1). Three Tegaderm films are printed with identical settings for each f_{mel} , in order to evaluate the reproducibility of the phantom fabrication process. For each f_{mel} , the attenuation and absorption coefficient spectra of one printed film are retrieved at five different locations to analyze the homogeneity of the phantoms.

Table 2. Overview of epidermal melanin phantoms: desired optical properties and corresponding printer input settings.^a

Phantom name	Desired values from literature [30]			Printer input settings				
	Melanosome volume fraction (%)	Absorption (μ_a) at 450 nm (mm^{-1})	Absorption (μ_a) at 550 nm (mm^{-1})	$O_{T,Y}$ (%)	$O_{T,M}$ (%)	$O_{Y,I}$ (%)	$O_{M,I}$ (%)	L
L0	0	0.2	0.1	0	0	0	0	0
L1	8	7.9	4.0	30	11	60	22	1
L1.5	12	11.7	6.0	45	16.5	60	22	1.5*
L2	16	15.6	8.0	60	22	60	22	2
L3	24	23.3	11.9	90	33	60	22	3
L4	32	31.0	15.9	120	44	60	22	4

^aPhotographs of the resulting phantoms are presented in Fig. 6. (* L1.5 was printed with two toner layers: the first toner layer with print opacity $O_p = 100\%$ and the second toner layer with $O_p = 50\%$.)

2.1.5. Application 2: spatially resolved photoacoustic phantoms

In this study, we develop thin, spatially resolved absorbing printed phantoms specifically designed for photoacoustic imaging applications. We present three distinct phantoms and explored two primary use cases. Firstly, we employed the phantoms to characterize a photoacoustic system, and secondly, we utilized them to acquire experimental photoacoustic images with digital ground truth. Additionally, we investigated the impact of tuning the optical properties of the phantom on the resulting photoacoustic signal. Detailed photographs of these three phantoms can be found in Section 3, accompanied by the corresponding results. All the photoacoustic phantoms were printed using black toner color, following the printing procedure explained earlier. A comprehensive photoacoustic imaging procedure is presented in subsection 2.2.4. The first phantom consisted of 14 printed disks with a diameter of 0.3 mm, arranged in a line with a center-to-center separation of 2.5 mm (Fig. 7(A)). This particular phantom served the purpose of characterizing the spatial variation of photoacoustic imaging using a linear transducer array. A maximum opacity level of 100% was selected for this phantom. The second set of phantoms comprised nine printed films, each featuring three disks with a diameter of 2 mm, arranged linearly with a center-to-center separation of 10 mm (Fig. 7(G)). These phantoms were designed to explore the tunability of optical properties for photoacoustic phantoms, considering spatial permutations of three different opacity levels: 33%, 66%, and 100%. Lastly, we utilized a widely used digital image of a vascular structure that was originally designed by Treeby et al. [41] to mimic blood vessels in a mouse brain. This digital vascular structure was printed with a maximum opacity level of 100% on a thin polyurethane film (Fig. 8(A)), serving the purpose of testing the accuracy of the proposed printing method in reproducing realistic blood vessel structures. Additionally, it allowed us to evaluate the photoacoustic image reconstruction from such structures.

2.2. Characterization and testing methods

Prior to all characterization measurements, the printed films were fixed on a slide projector frame using the intrinsic adhesive layer for the Tegaderm film and Scotch tape for the US cover. To ensure that the Tegaderm films were positioned in a reproducible manner, all films were slightly stretched uniformly in one direction from their original length of 35 mm to 40 mm using the slide projector frame as a reference.

2.2.1. Collimated transmission

A collimated transmission setup (Fig. 1(B)) was built to measure the attenuation spectra of the phantoms between 400–950 nm. The output spectrum of the light source (AvaLight-HAL-S-Mini, Avantes, The Netherlands) was guided through a 600 μm core optical fiber (FC-UVIR600-1-BX, Avantes, The Netherlands) and filtered by a blue glass filter in favor of the dynamic range towards the blue edge of the spectrum. Subsequently, it was collimated by two lenses ($f = 25.4$ mm, LA1951-A plano-convex, Thorlabs, USA) and guided through a 4.5 mm aperture (SM1D12, Thorlabs, USA), before it was transmitted through the phantom (sample). After interaction with the sample, the transmitted light was guided through two 4.5 mm apertures (SM1D12, Thorlabs, USA) that were 32 cm apart from each other. Finally, the light was coupled into a 400 μm core fiber (FT400EMT, Thorlabs, USA) that guided the light towards the detecting spectrograph (ULS2048CL-EVO-RS-UA, Avantes, The Netherlands).

The attenuation coefficient spectrum $\mu_t(\lambda)$ of the phantom was calculated using Beer's law as follows

$$\mu_t(\lambda) = -\frac{1}{d} \ln \left(\frac{I_T(\lambda) - I_{B,T}(\lambda)}{I_0(\lambda) - I_{B,0}(\lambda)} \right), \quad (5)$$

with $I_T(\lambda)$ the transmitted spectrum through the phantom (sample), $I_0(\lambda)$ the reference spectrum, $I_{B,T}(\lambda)$ and $I_{B,0}(\lambda)$ the background spectra for the sample and reference measurement, respectively, and d the thickness of the phantom. For all sample measurements, the reference spectrum $I_0(\lambda)$ was measured as the transmitted source spectrum through the collimated transmission setup without the presence of a sample. All background spectra $I_B(\lambda)$ were acquired by blocking the source light from reaching the detecting spectrograph. The thickness d of the phantom was obtained by OCT (Section 2.2.2) as the average d of 15 films.

The attenuation coefficient spectrum is composed of the sum of the scattering $\mu_s(\lambda)$ and absorption coefficient spectrum $\mu_a(\lambda)$ of the phantoms: $\mu_t(\lambda) = \mu_s(\lambda) + \mu_a(\lambda)$. For those toner colors with negligible absorption in the near-infrared region of the attenuation spectrum (yellow and magenta), the individual contributions of $\mu_s(\lambda)$ and $\mu_a(\lambda)$ were separated by least-squares fitting of a scatter power function to the scattering coefficient between 650 – 950 nm as

$$\mu_s(\lambda) = a\lambda^{-b}, \quad (6)$$

with free-running fit parameters a (scaling factor) and b (scatter power). Extrapolation of this scatter power function results in a scattering coefficient spectrum for the full wavelength range of 400 – 950 nm. Subsequently, $\mu_a(\lambda)$ can be obtained through

$$\mu_a(\lambda) = \mu_t(\lambda) - \mu_s(\lambda). \quad (7)$$

For those toner colors with non-negligible absorption in the near-infrared region of the attenuation spectrum (cyan and black), no separation of $\mu_s(\lambda)$ and $\mu_a(\lambda)$ was performed for this study.

2.2.2. Optical coherence tomography

A visible-light optical coherence tomography (OCT) system with a center wavelength of 550 nm and an axial resolution of 2.3 μm was used to characterize the thickness and refractive index of the polyurethane films, similar to the approach of Sorin and Gray [42]. The details of this home-built system are described in our previous work [43–45]. To quantify both thickness and refractive index, a small opening was cut in the phantom and it was placed on a glass slide, as schematically illustrated in Fig. 1(C). Subsequently, an OCT B-scan was made at the location of the edge of the opening of the phantom. The intensity peaks on the individual A-scans were fit to Gaussian functions and their locations were used to estimate the positions of surface reflections on the depth axis.

As shown in Fig. 1(C), the distance between the upper film surface reflection and the surface reflection of the glass plate in the opening was used to quantify the thickness of the phantom, d . Inside the phantom, the optical distance \mathcal{L} between the upper and bottom phantom surface is elongated with respect to the actual thickness d by the refractive index of the phantom material n , according to $\mathcal{L} = dn$. We used this relation and the previously found thickness d , to characterize the refractive index n of the films.

2.2.3. White light microscopy

A white light microscope (Zeiss Axiovert 200M, Carl Zeiss AG, Jena, Germany) with a 5 \times objective was used to evaluate the microscopic structure of the printed phantoms. The resulting images were analyzed using the Otsu method in MATLAB (MathWorks, version R2022b) to determine the surface coverage, which is defined as the percentage of the film covered with toner [46]. The Otsu method is based on image thresholding, which involves segmenting the image by minimizing the within-class variance of the pixels, resulting in a binary classification of the pixels as foreground (toner) or background (film).

2.2.4. Photoacoustic imaging

We utilized a handheld LED-based photoacoustic imaging system (Cyberdyne Inc., Japan) for our experiments. LED arrays consisting of 36×4 elements operating at a wavelength of 850 nm were employed as the light source, as previously reported [47,48]. Each LED array provided a pulse energy of 200 μJ with a pulse duration of 70 ns and a pulse repetition rate of 4 KHz. For acoustic detection, we employed a linear transducer array comprising 128 elements with a center frequency of 7 MHz and an 80% bandwidth. The imaging process involved averaging 2560 transducer sensor data to form the sinogram used for reconstruction. To reconstruct the photoacoustic images, we employed a Fourier domain reconstruction algorithm described by Jaeger et al. [49]. The optimal speed of sound for the reconstruction was empirically set to 1450 m s⁻¹ by reconstructing printed with point targets at multiple depths, utilizing the first photoacoustic phantom described in Section 2.1.5. This adjustment accounted for wave propagation through the polyurethane film and water-based tissue-mimicking medium. To facilitate visualization and comparison, both the ground truth and reconstructed images were normalized to their maximum values.

A 3D-printed phantom holder was utilized to ensure proper alignment of the phantoms within the imaging plane of the linear array, as depicted in Fig. 1(D) and (E). The phantom holder incorporated an attachment mechanism specifically designed to securely clamp the printed films, ensuring consistent and repeatable placement of the phantoms at the center of the transducer.

Two different photoacoustic imaging configurations were employed in this study. In the first configuration, the phantom holder was detached from the transducer, as illustrated in Fig. 1(D). Four LED arrays were stacked and affixed to the 3D-printed phantom holder, positioned at a distance of 15 mm from the printed phantom. The ultrasound transducer was mounted on a linear translational stage and separated from both the LED arrays and the phantom holder. This configuration enabled imaging of the phantom at various elevational distances from the transducer's imaging plane center. In the second configuration, the phantom holder was directly attached to the photoacoustic probe, as shown in Fig. 1(E). Two LED arrays were situated on either side of the transducer in a conventional manner. The second configuration allowed precise imaging of the phantom at the exact center of the imaging plane of the linear transducer array. All experiments were conducted by vertically aligning the film with the imaging plane of the linear array.

The first experiment aimed to study the elevational field-of-view and spatial variation of the photoacoustic signal. For this purpose, the first photoacoustic phantom, featuring 14 point targets along the depth direction (Fig. 7(A)), was utilized. To ensure uniform illumination of the targets,

we employed the first configuration described earlier, along with a scattering medium. The scattering medium was created by adding 220 ml of a 20% intralipid stock solution (Fresenius Kabi, Bad Homburg, Germany) to 4 liters of water in a glass tank, resulting in a reduced scattering coefficient of 10 cm^{-1} at 850 nm. Photoacoustic images were collected with elevational steps of $25 \text{ }\mu\text{m}$, covering a total scan distance of 10 mm. In the second set of experiments, phantoms P1 to P9 were positioned at the center of the imaging plane of the transducer. These phantoms were immersed in a tissue-mimicking medium with a reduced scattering coefficient of 10 cm^{-1} and an absorption coefficient of 0.1 cm^{-1} at 850 nm. To mimic the absorption, we added $59 \text{ }\mu\text{l}$ of India ink (Talens, The Netherlands) stock solution to the water with a dilution factor of 67796. The positioning of the phantoms along the depth direction was manually adjusted to maintain their location at 20 mm from the transducer within the focal zone. This set of experiments aimed to evaluate the change in photoacoustic signal for different levels of optical properties defined in phantoms P1 to P9. The optical attenuation coefficient for these opacity levels was obtained using the collimated transmission measurements as explained above. The third phantom, referred to as the vascular phantom, was imaged in a similar manner. The positioning of the phantom with respect to the transducer can be seen in Fig. 1(E). The vascular phantom was imaged under three different conditions: (i) in water, (ii) in a scattering medium with a reduced scattering coefficient of 10 cm^{-1} , and (iii) in a medium with both a reduced scattering coefficient of 10 cm^{-1} and an absorption coefficient of 0.1 cm^{-1} at 850 nm. These variations allowed us to assess the phantom's imaging performance in different optical environments.

The analysis of photoacoustic images was performed using the following procedures. For the first phantom with point targets, the lateral point spread functions were examined by extracting line profiles along the peak photoacoustic signal observed for each target. To assess the elevational field of view, a maximum intensity projection along the lateral direction for the elevational scans was generated, and the line profile passing through the peak value for each target was analyzed. To analyze the photoacoustic signal intensity for phantoms P1 to P9, a region of interest measuring $2 \text{ mm} \times 2 \text{ mm}$ was selected. The sum of pixel values within this region of interest was compared across the three opacity levels and attenuation coefficients. For the vascular phantoms, firstly, the reconstructed images were coregistered to the corresponding ground truth digital image. MATLAB Image Registration app was employed for image coregistration using features-based translation. The coregistered images were then evaluated using full-reference quality metrics, specifically the structural similarity index (SSIM) [50] and peak signal-to-noise ratio (PSNR), to assess the quality of the reconstructed images.

3. Results

3.1. Polyurethane film characterization

Figure 2(A) shows the average attenuation spectra of 15 unprinted polyurethane films for both film types (Tegaderm and US cover). With standard deviations (SDs) of $\pm 2 \text{ mm}^{-1}$ (5%; Tegaderm) and $\pm 0.36 \text{ mm}^{-1}$ (2%; US cover), the films are fairly reproducible in terms of optical attenuation. When assuming negligible absorption for the unprinted polyurethane films in this wavelength range ($0.001 - 0.005 \text{ mm}^{-1}$ [28]), the measured attenuation spectra approach the scattering coefficient spectra of the films. The measured values are similar to the reported scattering coefficients of various epithelial tissue types in the investigated spectral range, which range from approximately $2.2 - 50 \text{ mm}^{-1}$ [51]. Figures 2(B) and 2(D) show the microscopic structure of both polyurethane film types. Some dust particles and several mild inhomogeneities can be observed in the film material. The same films were printed with 0% opacity ($O_{T,j}$), which effectively means that it was sent through the printer without any active printing process. As can be observed in Figs. 2(C) and 2(E), this process introduces mild contamination with trace toner particles of all colors. Whereas those particles have no significant effect on the Tegaderm film

attenuation spectrum, they induce slight changes in attenuation for the US cover film (Fig. 2(A), dashed lines).

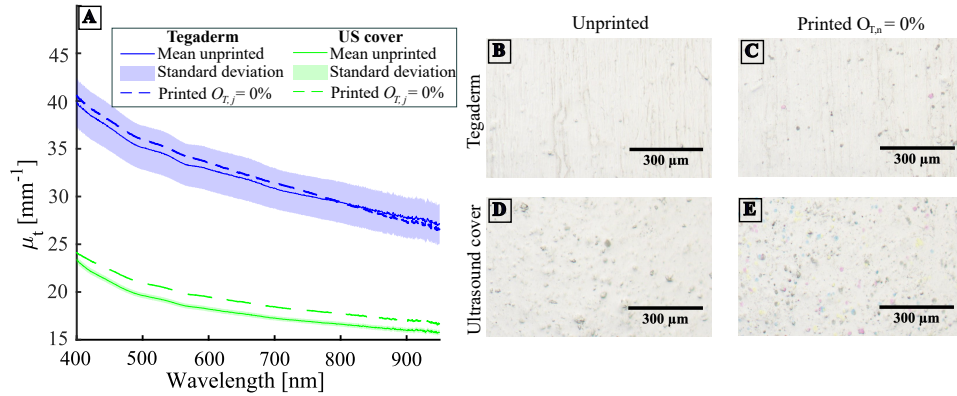


Fig. 2. (A) Average attenuation spectra (solid lines) and standard deviation (shaded areas) of 15 unprinted polyurethane films for both film types (Tegaderm and US cover). The dashed lines present the attenuation spectra of both film types after printing with an opacity $O_{T,j}$ of 0% (no active printing process). (B) and (D) Microscopic images of the unprinted Tegaderm and US cover, respectively. (C) and (E) Microscopic images of the Tegaderm and US cover, respectively, after printing with an opacity $O_{T,j}$ of 0% (no active printing process). The scale bar size is 300 μm for all microscopy images.

The OCT evaluation of 15 unprinted films for both film types (Tegaderm and US cover) resulted in a thickness of $39.2 \pm 3.0 \mu\text{m}$ (Tegaderm; average \pm SD) and $57.0 \pm 7.7 \mu\text{m}$ (US cover). The resulting refractive indices were 1.71 ± 0.10 (Tegaderm) and 1.47 ± 0.04 (US cover). For the Tegaderm films only, we observed a bi-layer structure in the OCT images. This finding can be attributed to the adhesive layer that is present on top of the polyurethane layer in the Tegaderm films.

3.2. Printed polyurethane films

Figures 3(A), C, E, and G, present the results of the attenuation coefficient spectra of the Tegaderm films with pure toner colors (Y, M, C, and K) for different opacities $O_{T,j}$. Figures 3(B), D, F, and H, show that the attenuation increases linearly with opacity at the absorption peak for each toner color. Linear fits of the type $\mu_t = \alpha O_{T,j} + \beta$ through the data in Fig. 3(B), (D), (F), and (H) (solid lines) resulted in fit coefficients $\alpha = [0.61, 0.68, 0.42, 0.75]$ and $\beta = [30.0, 32.4, 34.1, 18.9]$ for yellow, magenta, cyan and black, respectively. The insets show the microscopic structure of the printed films at an opacity of 50% for each color, with observable clusters of toner particles that are approximately 100 μm in diameter. Similar to Fig. 2(C) and (E), mild contamination with trace particles of other toner colors can be observed in each microscopy image.

Figure 4(A) shows how the microscopic structure changes with opacity. Up to $O_{T,j} = 100\%$ opacity, individual clusters of toner particles can be observed, which increase in size with increasing opacity. For opacities of 100% and beyond, no individual clusters are recognizable, but color intensity increases further with opacity. For opacities $O_{T,j} < 100\%$, we analyzed the surface coverage as the percentage of the image area that contains magenta toner particles using the Otsu method (Section 2.2.3). A linear relationship between the surface coverage and opacity can be observed in Fig. 4(B). The OCT evaluation of these printed films indicated that there was no significant change in film thickness and refractive index after printing. This suggests that the layer of toner particles is thinner than the axial resolution of the OCT system (2.3 μm). For the pure colors yellow and magenta, the measured attenuation coefficients were corrected

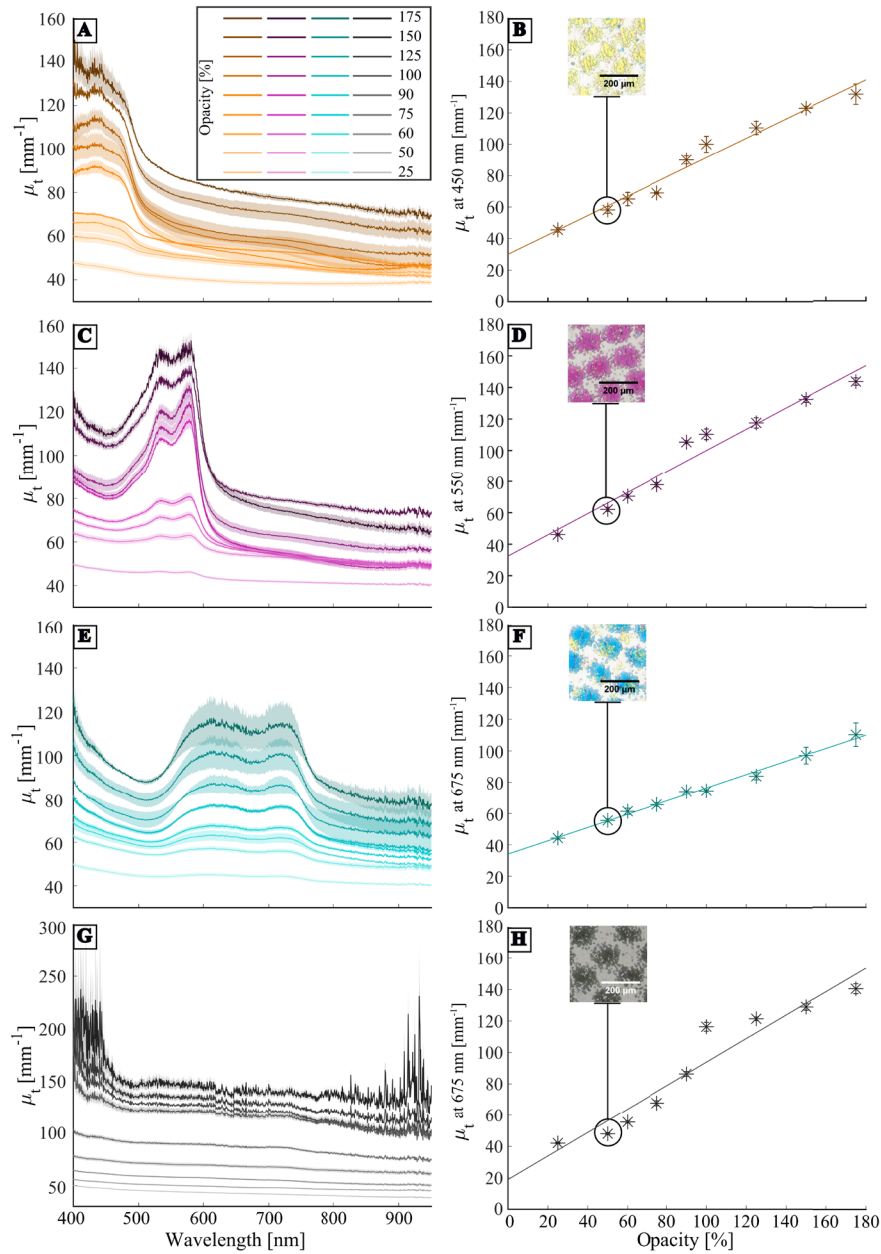


Fig. 3. Attenuation spectra for different opacities ($O_{T,j}$) of the printed polyurethane films (Tegaderm) with pure toner colors: (A) yellow, (C) magenta, (E) cyan, (G) black. Solid lines present the average attenuation spectrum per opacity $O_{T,j}$, and shaded areas around the line present the standard deviation of μ_t for 3 independently printed films. Average attenuation coefficient and standard deviation (error bar) versus opacity $O_{T,j}$ around the center of the attenuation peak: (B) yellow (445 – 455 nm), (D) magenta (545 – 555 nm), (F) cyan (670 – 680 nm), (H) black (670 – 680 nm). Solid lines in (B), (D), (F), and (H) represent linear fits of the data. Insets show the microscopic structure of the printed films at an opacity of $O_{T,j} = 50\%$ for each color. The scale bar size is 200 μ m for all microscopic images.

for the scattering contribution using Eqs. (6) and (7). Figure 5(A) presents the fitted scattering contribution (dashed lines) for an opacity $O_{T,j}$ of 100%. The resulting absorption coefficient spectra are shown in Fig. 5(B). Figures 5(C) and (D) show the absorption coefficients as a function of opacity for yellow and magenta, respectively. Linear fits of the type $\mu_t = \alpha O_{T,j} + \beta$ through the data in solid lines in Fig. 5(C) and (D) resulted in fit coefficients $\alpha = [0.28, 0.41]$ and $\beta = [-4.9, -7.5]$ for yellow and magenta, respectively. In comparison to the attenuation coefficient fits (Fig. 3(B), (D), (F), and (H)), the absorption coefficient fits are close to crossing the origin of the plots (Fig. 5(C) and (D)). This indicates a reasonable correction for the scattering contribution to the attenuation coefficients of the yellow and magenta toner.

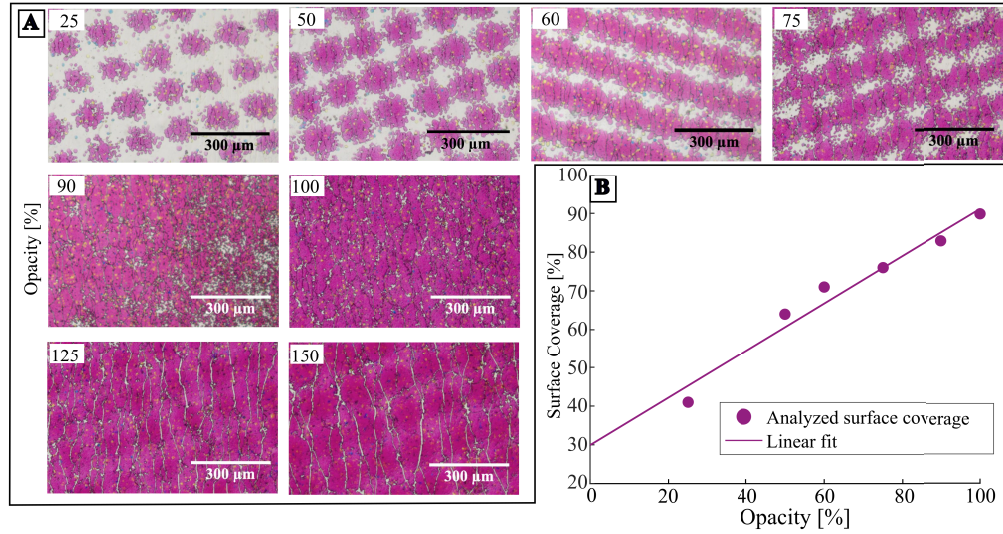


Fig. 4. (A) Microscopic structure of printed films at different opacities $O_{T,j}$ for pure magenta. The scalebar is 300 μm for all images. (B) Surface coverage versus opacity $O_{T,j}$ for opacities up to 100%.

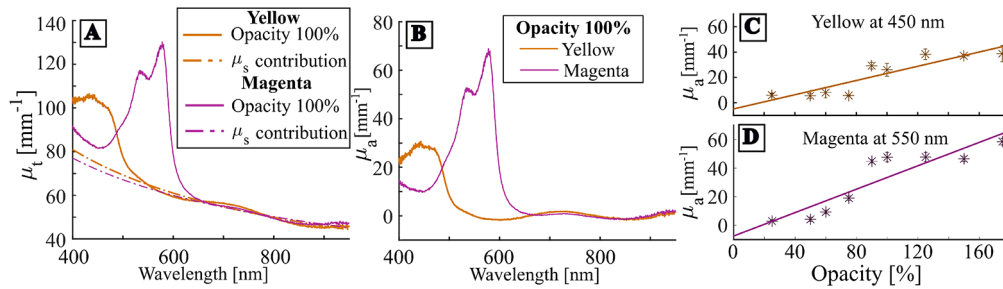


Fig. 5. (A) Attenuation coefficient spectra of the printed Tegaderm films for yellow and magenta ($O_{T,j} = 100\%$) with corresponding scatter power fits using Eq. (6). (B) Absorption coefficient spectra for yellow and magenta ($O_{T,j} = 100\%$), obtained using Eq. (7). (C) and (D) absorption coefficient versus opacity ($O_{T,j}$) for yellow and magenta, respectively. Solid lines present linear fits.

3.3. Application 1: homogeneous epidermal melanin phantoms

Figure 6 displays the microscopic appearance and absorption coefficient spectra of a series of six epidermal melanin phantoms as specified in Table 2. Since these phantoms were printed with yellow and magenta toner only, the μ_a was retrieved using Eqs. (6) and (7). The phantoms mimic six different melanosome volume fractions f_{mel} , for which the literature spectra that optimally match the measured absorption are presented with dashed lines [30]. Note that the phantom absorption is matched with the desired literature values at only two wavelengths (450 and 550 nm), as these are the wavelengths at which commercial transcutaneous bilirubin meters operate. For all mimicked f_{mel} , a slight difference exists between the target f_{mel} (Table 2: 0%, 8%, 12%, 16%, 24%, 32%) and the f_{mel} that best matches the measured phantom absorption at 450 and 550 nm (Fig. 6: 0%, 5%, 11%, 19%, 28%, 40%). For phantoms L0, L1, L1.5, L2, and L3, these differences amount maximally 4%, which can be ascribed to the inaccuracy of the printing process. For the highest mimicked f_{mel} in phantom L4, the difference between the target and printed f_{mel} amounts to 8%, which can additionally be ascribed to the limitations in the dynamic range of the collimated transmission setup for measuring high absorption values.

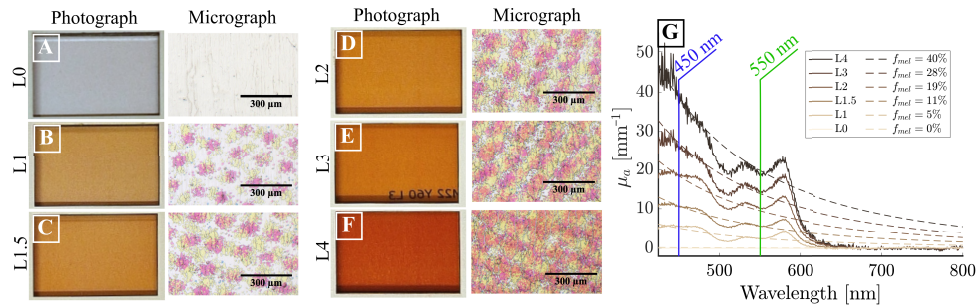


Fig. 6. (A-F) Photographs ($35 \times 23 \text{ mm}^2$) and microscopic structure (scale bar $300 \mu\text{m}$) for the six epidermal phantoms that mimic a range of melanosome volume fractions f_{mel} at 450 and 550 nm, as specified in Table 2. (G) Absorption coefficient spectra for all phantoms (solid lines). Dashed lines present the literature values that best match the measured f_{mel} , which differ slightly from the target f_{mel} in Table 2 due to inaccuracies in the printing process and the limited dynamic range of the collimated transmission setup for high absorption values. Vertical lines at 450 and 550 nm highlight the wavelengths at which the phantom absorption was matched with the literature values.

The reproducibility of the printing process for these epidermal melanin phantoms was evaluated by printing three individual films per mimicked f_{mel} . The standard deviation of the absorption coefficient over these three phantoms ranged between 14.7 – 32.9% of the average μ_a at 450 and 550 nm. Variations between films in the polyurethane film material, film preparation, and the printing process contribute to this variation. The homogeneity of the printing process for these epidermal melanin phantoms was evaluated by examining the spatial variation in μ_a at five different locations in each phantom. The standard deviation of μ_a within a single phantom ranged between 8.4 – 23.8%. Spatial variations within films in polyurethane material and disuniform printing contribute to this variation.

3.4. Application 2: photoacoustic phantoms

Figure 7(A) presents a photograph of the printed phantom featuring fourteen point targets. In Figs. 7(B), (C), and (D), we observe photoacoustic images of the point targets positioned at -2.5 mm , 0 mm , and 2.5 mm relative to the presumed transducer center, respectively. For a comprehensive analysis, Fig. 7(E) exhibits a stacked plot of line profiles along the lateral direction

(axis along the transducer elements) for all the observed targets in the photoacoustic images. Notably, the line profiles represent the peak values of the point targets and are normalized for optimal visualization. The red dashed line in Fig. 7(E) illustrates the contour plot representing the full-width half maximum (FWHM) of the observed point spread functions (PSFs). Additionally, the elevational field of view is depicted in the stacked plot of Fig. 7(F), which demonstrates the normalized maximum intensity projection along the lateral direction as a function of the elevational distance from the center of the imaging plane. The red dashed line in Fig. 7(F) illustrates the contour plot representing the FWHM.

By orienting the film vertically in the imaging plane of the linear array, we obtained an estimate of the transducer center by linearly translating the transducer and determining the location where the photoacoustic signal reached its maximum for all the targets. Figure 7(C) illustrates this observation, where the photoacoustic signal peaks for targets 4 to 7 within the transducer's focal

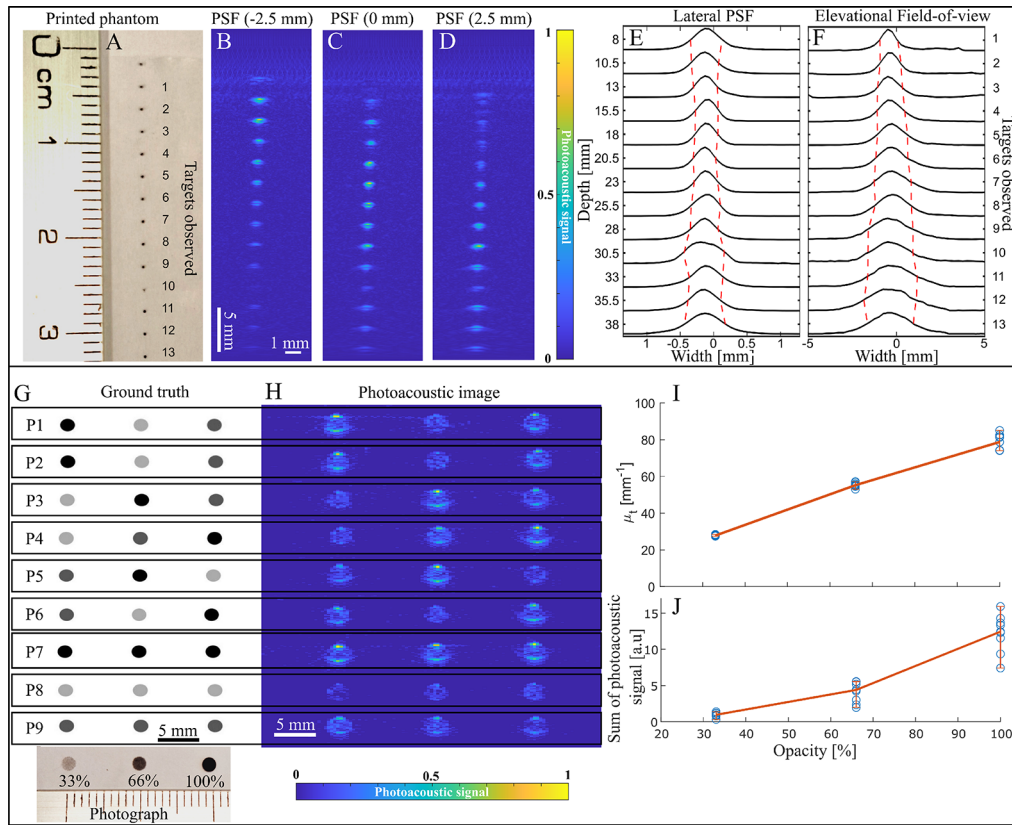


Fig. 7. (A) Photograph of the printed phantoms showcasing point targets at various depths. (B) Point spread function (PSF) at -2.5 mm from the estimated center of the transducer. (C) PSF at the presumed transducer center. (D) PSF at 2.5 mm from the transducer center. (E) Lateral line profile through PSF for targets at different depths. (F) Elevational field of view plot indicating peak signal intensity at varying distances from the transducer center. (G) Ground truth image of nine printed disc phantoms (P1 - P9) with permutations of different opacity levels ($O_{T,j} = 33, 66, \text{ and } 100\%$). Photograph of one of the phantoms at the bottom (H) Corresponding photoacoustic images of phantoms (P1 - P9). (I) The plot of optical attenuation coefficient measurements on printed films against opacity levels. (J) The sum of the photoacoustic signal within the disk regions of interest for the nine phantoms (P1 - P9) corresponds to the three opacity levels.

zone along the depth direction. In Figs. 7(B) and 7(D), we can observe that the photoacoustic signal deteriorates as the distance from the center increases, with maximum signal intensities observed for off-focal targets 2-3 and 8-13. Furthermore, Figs. 7(B), (C), and (D) clearly show that narrow PSFs are obtained along the lateral direction within the transducer's focal zone, while the PSFs become broader for targets on both sides of the focal zone. This aspect is highlighted in Fig. 7(E) through the contour plot overlaid on the lateral PSFs. The FWHM of the targets varies from 0.46 mm for target 1 (at a depth of 8 mm) to a minimum of 0.33 mm for target 6 (at a depth of 20.5 mm) within the focal zone and increases to 0.61 mm for target 13 (at a depth of 38 mm). Here, we consider the range of the best FWHM values observed from 0.33 mm to 0.35 mm to define the transducer's focal zone, where it achieves high resolution. Figure 7(F) demonstrates that as the target moves farther away from the transducer, more out-of-plane signals are collected. Interestingly, the FWHM increases from 1 mm for target 1 (at a depth of 8 mm) close to the transducer, to 3 mm for target 13 (at a depth of 38 mm) further away from the transducer. This indicates that a linear array collects the photoacoustic signal over a wider range than an ideal 2D imaging plane, and the contribution of out-of-plane signals increases with depth.

Figure 7(G) shows nine disk phantoms (P1 to P9), each having three opacity levels: 33%, 66%, and 100%. Figure 7(H) are the corresponding reconstructed photoacoustic images. As shown in Fig. 7(G), phantoms with 100% opacity have the highest photoacoustic signal intensity, followed by 66% and 33% opacity. The optical attenuation coefficient of the three opacity level phantoms is shown in Fig. 7(I) with a mean value of 27.9, 55.3, and 79 mm^{-1} for $O_P = 33, 66$, and 100% at 850 nm respectively. The sum of the photoacoustic signal of each disk phantom against opacity levels is presented in Fig. 7(J).

Opacity levels and total attenuation coefficient show a linear relation with an R^2 of 0.985. Assuming the ink particles are dominantly absorbing and have minimal scattering contribution with an increase in opacity, the optical absorption coefficient changes linearly with the opacity levels. The photoacoustic signal is directly proportional to the optical absorption for a constant light fluence. This aspect is depicted in Fig. 7(J), as the photoacoustic signal intensity increases with the opacity levels. The mean photoacoustic signal from the discs increased as the opacity level increased from 33% to 66% and 100%, with values of 1, 4, and 12, respectively. However, there was some deviation in the measurements, which might be due to the positioning of the phantom along the depth and the imaging plane.

Figure 8(A) presents a photograph of the printed vascular phantom. Figures 8(B), (C), and (D) display the photoacoustic images acquired with the film positioned vertically, at the imaging plane of the linear transducer array. Figure 8(B) illustrates the imaging of the phantom in water, while Fig. 8(C) demonstrates imaging in a scattering medium with a reduced scattering coefficient of $\mu'_s = 10 \text{ cm}^{-1}$. Figure 8(D) exhibits imaging in a scattering and absorbing medium with a reduced scattering coefficient of $\mu'_s = 10 \text{ cm}^{-1}$ and an absorption coefficient of $\mu_a = 0.1 \text{ cm}^{-1}$. In Fig. 8(E), an overlaid image is presented, depicting the ground truth vascular phantom in blue along with the photoacoustic image from Fig. 8(B). The spatial misalignment of the experimental image is visibly apparent. Finally, Fig. 8(F) illustrates the coregistered image, displaying the overlapping ground truth and experimental images.

The results depicted in Fig. 8 emphasize the advantage of employing this phantom, as it enables the acquisition of experimental images with accurate digital ground truth for structurally complex phantoms. Moreover, these results demonstrate the versatility of the phantom approach, facilitating imaging in various mediums with different optical properties. Figure 8(B), (C), and (D) exemplify this capability by presenting images obtained in water, a scattering medium, and a combined scattering and absorbing medium, respectively. It is noticeable from these images that the optimal imaging depth is achieved in water, followed by the scattering medium, and the least optimal depth is achieved in the combined absorbing and scattering medium. By setting a noise threshold of 0.02 on the normalized images, the deepest targets observed were 29.2 mm in

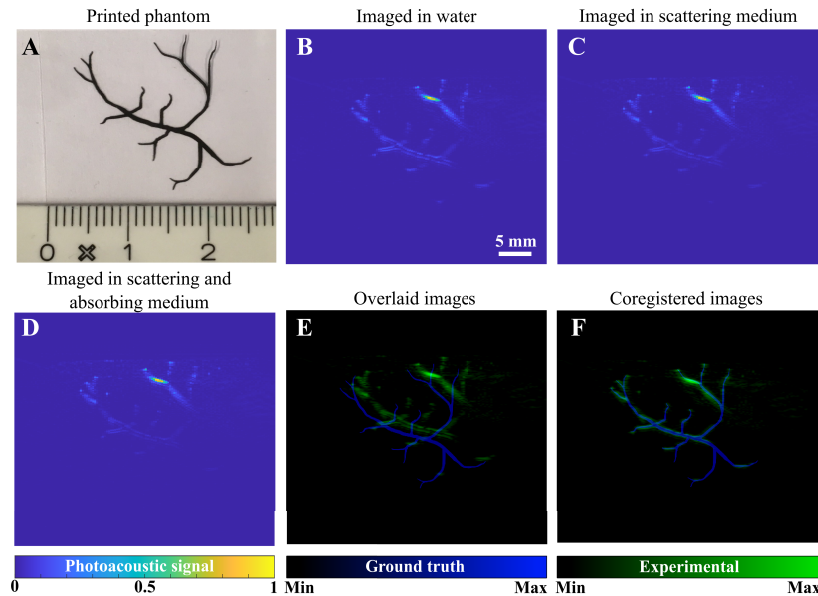


Fig. 8. (A) Photograph of the printed vascular phantom. (B) Photoacoustic image of the phantom positioned in the transducer's imaging plane, using water as the medium. (C) Photoacoustic image of the phantom within a scattering medium with a reduced scattering coefficient of $\mu'_s = 10 \text{ cm}^{-1}$. (D) Photoacoustic image of the phantom within a medium with a reduced scattering coefficient of $\mu'_s = 10 \text{ cm}^{-1}$ and an absorption coefficient of $\mu_a = 0.1 \text{ cm}^{-1}$. (E) Overlay of the ground truth image (blue) and the experimental image (green) from (B). (F) Coregistered ground truth (blue) and experimental (green) images.

water, 26.9 mm in the scattering medium, and 23.6 mm in the combined absorbing and scattering medium. The SSIM values for the images, compared to the ground truth, in these three mediums are 0.90, 0.88, and 0.86, respectively. Additionally, the PSNR values are 18.38, 18.11, and 17.93, respectively. These quality metrics were presented to demonstrate that the proposed approach enables us to make a direct comparison with the ground truth digital image. Although the SSIM and PSNR values exhibit a decrease when scattering and absorption are present in the medium, the changes are not drastic due to the sparse nature of the imaged structure.

4. Discussion

In this paper, we presented a new methodology to fabricate thin phantoms with absorption properties that are controllable in magnitude, spectral shape, and spatial distribution. We developed a model to predict the optical properties of the phantoms based on the input settings of the printer and we demonstrated the feasibility of our method for two relevant applications in biomedical optics research. The most important asset and novelty of our methodology is its accessibility, as it only requires a standard office laser printer and polyurethane films that are low-cost and commonly available. As demonstrated in this study, the optical attenuation and absorption of the printed films can be estimated based on the printer input settings (opacity). This further facilitates a systematic phantom design. We expect that these thin phantoms can have a valuable impact on biomedical optics research since they are less time-consuming and inexpensive to fabricate compared to other methods that are currently available [1–6]. For the appropriate application of our methodology, it is also important to consider its limitations, as well as other considerations for successful implementation. In the remaining part of this discussion section, we provide an overview of these aspects.

4.1. Controllability of optical properties

The optical absorption of the phantoms is controllable by tuning the opacity of the toner colors (C, M, Y, K). It is important to note that the resulting absorption spectrum of the phantoms is limited to a linear combination of the absorption spectra of the four toner colors. This poses no problem for applications with only a few wavelengths in the visible wavelength range, such as the example of epidermal melanin phantoms for transcutaneous bilirubin measurements given in this paper. However, this method is less suited to accurately mimic broadband absorption spectra with detailed absorption features.

The optical scattering properties of the phantoms fully depend on the scattering properties of the polyurethane film and the toner. As such, control over the optical scattering properties is limited to the choice of polyurethane film. The polyurethane films that were used in this paper differed substantially in optical scattering (Fig. 2), but optical scattering was fairly reproducible between polyurethane films of the same type. In favor of biomedical applications, the optical scattering properties of the polyurethane films are within the biological range of tissue scattering [30,52].

4.2. Optical property characterization

Although the phantom optical properties are predictable with reasonable reproducibility by using the model proposed in this study, an exact estimate may be required in many experimental situations. We, therefore, advise to always evaluate the optical properties of the phantoms after printing. We used a collimated transmission setup for this purpose, which allows for measuring the total optical attenuation coefficient of the phantoms. Separation of the absorption and scattering contribution was achieved by fitting a scatter power function to the non-absorbing part of the attenuation spectrum (650 – 950 nm) for those toner colors with negligible absorption in the near-infrared region of the attenuation spectrum (yellow and magenta). To also separate the absorption and scattering contribution of toner colors with non-negligible absorption in this wavelength region (cyan and black), other characterization methods can be employed, such as Kubelka Munk theory [53] and the inverse adding doubling method [54,55]. Using these more advanced analysis methods will potentially allow correction of the layered distribution of the polyurethane film and the toner color layer, which is not taken into account with the collimated transmission. From the OCT characterization, the measured refractive index of Tegaderm (1.71) is higher than the expected refractive index for polyurethane (1.41 – 1.58) [29]. This finding may be ascribed to the presence of the adhesive layer in this film. Since the composition and the refractive index of the adhesive are unknown, we used the measured value which comprises both layers. Please note that this finding does not affect the measurement of the film thickness d , which was measured independently of the refractive index (Fig. 1(C)). The measured refractive index of the US cover (1.47) was within the expected range.

4.3. Microscopic structure

As can be observed in Fig. 4(A), the printing process induces inhomogeneities in toner distribution on a microscopic scale with toner clusters of approximately 100 μm in diameter up to a print opacity of 100%. This clustered distribution of absorption will affect light propagation on a microscopic level. For measurement geometries that are sensitive to the microscopic scale, this will need to be accounted for. However, for the collimated transmission measurements in this study (illumination beam diameter of 4.5 mm), the spatial variation in optical absorption within individual printed phantoms was relatively small. For the application of transcutaneous bilirubin measurements, a similar argument holds for the diffusely scattered light that is collected by the bilirubin meter (Draeger JM-103 and JM-105) in a circular detection geometry with source-detector separations that range between 1.9 mm and 5.3 mm. Also, for the photoacoustic imaging application, the toner cluster separation is smaller than the spatial resolution of the

system (0.3 – 0.4 mm). The microscopic analysis in this study did not provide information on how the toner particles are distributed in 3D when printed on polyurethane films. Since the melting temperature of polyurethane (180°C) is close to the fuser temperature of the printer (175°C), toner particles might be encapsulated by the film material. This could not be confirmed by the OCT analysis of the printed films, due to limitations in spatial resolution.

4.4. Practical considerations

As the methodology of this study is based on the use of a standard office laser printer, it is expected that printer type, toner type, and potentially other factors (printer age, maintenance, toner availability, etc.) will affect the optical properties of the printed phantoms. We advise to always evaluate the optical properties of the phantoms after printing. Some types of laser printers add a machine identification code (MIC) to the printed area: a digital watermark of a certain toner color to allow for identification of the printing device. No signature of MIC was observed in the optical properties in this study. However, as shown in Fig. 2, the printer introduced mild contamination with trace toner particles of all colors, even if no print assignment was applied (opacity $O_{T,j} = 0\%$). If desired, this contamination can potentially be avoided by removing those toner cartridges that are not required for phantom printing.

4.5. Epidermal melanin phantoms

The epidermal melanin phantoms that were fabricated in this study are of particular interest for the evaluation of the influence of skin pigmentation on transcutaneous bilirubin measurements in newborns. As literature values for adult skin pigmentation were used as a reference in this study, potential differences between adult skin pigmentation and newborn skin pigmentation should be taken into account. Optimization of phantom absorption for other wavelengths also opens possibilities to evaluate the influence of skin pigmentation for other optical modalities, for example in pulse oximetry. The adhesive layer that is intrinsically present in the Tegaderm films also has the potential to assist *in-vivo* evaluations, by applying the printed phantoms directly on living skin.

4.6. Photoacoustic imaging phantoms

This study highlights our achievement in developing photoacoustic phantoms from digital ground truth images, as demonstrated in Fig. 8. As the application of photoacoustic imaging expands toward clinical settings, the importance of quantitative imaging continues to grow. Consequently, it becomes imperative to evaluate these methods using phantoms that encompass a wide range of tissue optical properties and exhibit complex tissue structures, while also providing accurate ground truth information. The proposed phantom can be a potential candidate in this direction with tunable optical properties. In our work, we successfully demonstrated two unique use cases of this phantom. Firstly, we utilized the phantom to determine the elevational field-of-view, as exemplified in Fig. 7. This application showcases the versatility of the phantom in characterizing a photoacoustic imaging system. The amount of out-of-plane signal with depth as shown in Fig. 7 can help to analyze photoacoustic images and might provide useful information to correct for related artifacts. Secondly, we employed the phantom to obtain coregistered experimental images, enabling direct comparison with the ground truth digital image, as depicted in Fig. 8. By aligning the experimental images with the ground truth, one could assess the image quality to optimize the system parameters.

However, this method does have some limitations. One major drawback is the thin nature of the phantoms in this study. In photoacoustic imaging, particularly when utilizing a vertically-oriented thin phantom in the imaging plane, there are limitations in its ability to accurately mimic actual tissue characteristics. In reality, photoacoustic imaging that employs a linear array is inherently three-dimensional, involving both light interaction and acoustic detection from a larger volume

beyond the ideal imaging plane. While the light interaction can be faithfully replicated, the acoustic propagation from a thin film will not be identical to that from a three-dimensional structure. Although this aspect may pose limitations for certain organ-mimicking applications, the thin-printed phantoms can be highly valuable for the characterization and optimization of imaging systems, testing of image reconstruction, and quantification algorithms.

5. Conclusion

We introduced a user-friendly method to systematically design and fabricate thin phantoms with controllable absorption properties using a standard office laser printer and polyurethane films. We characterized the optical and geometrical properties of the polyurethane films and the printed phantoms, using collimated transmission, optical coherence tomography, white light microscopy, and photoacoustics. The characterization of the thin phantoms in terms of optical properties and reproducibility of the printing process highlights the potential of our approach for biomedical research and development. We demonstrated two potential applications: *i*) homogeneous epidermal melanin phantoms and *ii*) spatially resolved absorbers for photoacoustic imaging. Overall, this approach provides a promising alternative to traditional phantom fabrication methods that are often complex, expensive, and time-consuming.

Funding. Dutch Research Council (NWO) (19165); European Research Council (101040376); Netherlands Organ-on-Chip Initiative (024.003.001).

Disclosures. The authors have no financial interests or conflict of interest to disclose.

Data availability. The data sets produced and studied in this manuscript are available by contacting the corresponding author upon prior request.

References

1. D. Gorpas, H. Wabnitz, and T. J. Pfefer, "Special section guest editorial: Tissue phantoms to advance biomedical optical systems," *J. Biomed. Opt.* **27**(07), 1 (2022).
2. J. Palma-Chavez, T. J. Pfefer, A. Agrawal, J. V. Jokerst, and W. C. Vogt, "Review of consensus test methods in medical imaging and current practices in photoacoustic image quality assessment," *J. Biomed. Opt.* **26**(09), 090901 (2021).
3. J. Chue-Sang, M. Gonzalez, A. Pierre, M. Laughrey, I. Saytashev, T. Novikova, and J. C. Ramella-Roman, "Optical phantoms for biomedical polarimetry: a review," *J. Biomed. Opt.* **24**(03), 1 (2019).
4. G. Lamouche, B. F. Kennedy, K. M. Kennedy, C.-E. Bissillon, A. Curatolo, G. Campbell, V. Pazos, and D. D. Sampson, "Review of tissue simulating phantoms with controllable optical, mechanical and structural properties for use in optical coherence tomography," *Biomed. Opt. Express* **3**(6), 1381 (2012).
5. B. W. Pogue and M. S. Patterson, "Review of tissue simulating phantoms for optical spectroscopy, imaging and dosimetry," *J. Biomed. Opt.* **11**(4), 041102 (2006).
6. A. B. Walter and E. D. Jansen, "Development of a platform for broadband, spectra-fitted, tissue optical phantoms," *J. Biomed. Opt.* **28**(02), 025001 (2023).
7. M. Dantuma, S. Kruitwagen, J. Ortega-Julia, R. P. Pompe van Meerdervoort, and S. Manohar, "Tunable blood oxygenation in the vascular anatomy of a semi-anthropomorphic photoacoustic breast phantom," *J. Biomed. Opt.* **26**(03), 036003 (2021).
8. W. Yim, J. Zhou, L. Sasi, J. Zhao, J. Yeung, Y. Cheng, Z. Jin, W. Johnson, M. Xu, J. Palma-Chavez, L. Fu, B. Qi, M. Retout, N. J. Shah, J. Bae, and J. V. Jokerst, "3d-bioprinted phantom with human skin phototypes for biomedical optics," *Adv. Mater.* **35**(3), 2206385 (2023).
9. L. A. Dempsey, M. Persad, S. Powell, D. Chitnis, and J. C. Hebden, "Geometrically complex 3d-printed phantoms for diffuse optical imaging," *Biomed. Opt. Express* **8**(3), 1754 (2017).
10. G. T. Kennedy, G. R. Lentsch, B. Trieu, A. Ponticorvo, R. B. Saager, and A. J. Durkin, "Solid tissue simulating phantoms having absorption at 970 nm for diffuse optics," *J. Biomed. Opt.* **22**(7), 076013 (2017).
11. L. Hacker, J. Joseph, A. M. Ivory, M. O. Saed, B. Zeqiri, S. Rajagopal, and S. E. Bohndiek, "A copolymer-in-oil tissue-mimicking material with tuneable acoustic and optical characteristics for photoacoustic imaging phantoms," *IEEE Transactions on Medical Imaging* **40**(12), 3593–3603 (2021).
12. W. C. Vogt, X. Zhou, R. Andriani, K. A. Wear, T. J. Pfefer, and B. S. Garra, "Photoacoustic oximetry imaging performance evaluation using dynamic blood flow phantoms with tunable oxygen saturation," *Biomed. Opt. Express* **10**(2), 449 (2019).
13. J. Park, M. Ha, S. Yu, and B. Jung, "Fabrication of various optical tissue phantoms by the spin-coating method," *J. Biomed. Opt.* **21**(6), 065008 (2016).
14. A. Curatolo, B. F. Kennedy, and D. D. Sampson, "Structured three-dimensional optical phantom for optical coherence tomography," *Opt. Express* **19**(20), 19480 (2011).

15. P. Diep, S. Pannem, J. Sweer, J. Lo, M. Snyder, G. Stueber, Y. Zhao, S. Tabassum, R. Istfan, J. Wu, S. Erramilli, and D. Roblyer, "Three-dimensional printed optical phantoms with customized absorption and scattering properties," *Biomed. Opt. Express* **6**(11), 4212 (2015).
16. A. I. Chen, M. L. Balter, M. I. Chen, D. Gross, S. K. Alam, T. J. Maguire, and M. L. Yarmush, "Multilayered tissue mimicking skin and vessel phantoms with tunable mechanical, optical, and acoustic properties," *Med. Phys.* **43**(6Part1), 3117–3131 (2016).
17. P. Urso, M. Lualdi, A. Colombo, M. Carrara, S. Tomatis, and R. Marchesini, "Skin and cutaneous melanocytic lesion simulation in biomedical optics with multilayered phantoms," *Physics in Medicine Biology* **52**(10), N229–N239 (2007).
18. L. C. Ikejimba, C. G. Graff, S. Rosenthal, A. Badal, B. Ghammraoui, J. Y. Lo, and S. J. Glick, "A novel physical anthropomorphic breast phantom for 2d and 3d x-ray imaging," *Med. Phys.* **44**(2), 407–416 (2017).
19. P. Jahnke, F. R. Limberg, A. Gerbl, G. L. Ardila Pardo, V. P. Braun, B. Hamm, and M. Scheel, "Radiopaque three-dimensional printing: a method to create realistic ct phantoms," *Radiology* **282**(2), 569–575 (2017).
20. J. P. Cruz-Bastida, E. L. Marshall, N. Reiser, J. George, E. A. Pearson, K. A. Feinstein, H. A. Al-Hallaq, C. S. Burton, D. Beaulieu, R. D. MacDougall, and I. Reiser, "Development of a neonate x-ray phantom for 2d imaging applications using single-tone inkjet printing," *Med. Phys.* **48**(9), 4944–4954 (2021).
21. R. A. Kruger, C. M. Kuzmiak, R. B. Lam, D. R. Reinecke, S. P. Del Rio, and D. Steed, "Dedicated 3d photoacoustic breast imaging," *Med. Phys.* **40**(11), 113301 (2013).
22. M. W. Sjöding, R. P. Dickson, T. J. Iwashyna, S. E. Gay, and T. S. Valley, "Racial bias in pulse oximetry measurement," *N. Engl. J. Med.* **383**(25), 2477–2478 (2020).
23. B. O. Olusanya, D. O. Imosemi, and A. A. Emokpae, "Differences between transcutaneous and serum bilirubin measurements in black African neonates," *Pediatrics* **138**(3), 1 (2016).
24. Y. Mantri and J. V. Jokerst, "Impact of skin tone on photoacoustic oximetry and tools to minimize bias," *Biomed. Opt. Express* **13**(2), 875–887 (2022).
25. A. Afshari, R. B. Saager, D. Burgos, W. C. Vogt, J. Wang, G. Mendoza, S. Weininger, K.-B. Sung, A. J. Durkin, and T. J. Pfeifer, "Evaluation of the robustness of cerebral oximetry to variations in skin pigmentation using a tissue-simulating phantom," *Biomed. Opt. Express* **13**(5), 2909–2928 (2022).
26. N. Evans and N. Rutter, "Development of the epidermis in the newborn," *Neonatology* **49**(2), 74–80 (1986).
27. M. Dantuma, S. Kruitwagen, J. O. Julia, R. P. van Meerdervoort, and S. Manohar, "Imaging results from a semi-anthropomorphic photoacoustic-ultrasound breast phantom carrying blood vessels," in *European Conference on Biomedical Optics*, (Optica Publishing Group, 2021), pp. ETu5B-4.
28. T. Moffitt, Y.-C. Chen, and S. A. Prahl, "Preparation and characterization of polyurethane optical phantoms," *J. Biomed. Opt.* **11**(4), 041103 (2006).
29. E. Ortyl, S. Kucharski, and T. Gotszalk, "Refractive index modulation in the polyurethane films containing diazo sulfonamide chromophores," *Thin Solid Films* **479**(1-2), 288–296 (2005).
30. S. L. Jacques, "Optical properties of biological tissues: a review," *Physics in Medicine Biology* **58**(11), R37–R61 (2013).
31. Y. Liu and S. Maruvada, "Development and characterization of polyurethane-based tissue and blood mimicking materials for high intensity therapeutic ultrasound," *J. Acoust. Soc. Am.* **151**(5), 3043–3051 (2022).
32. H. Azhari, *Basics of Biomedical Ultrasound for Engineers* (John Wiley & Sons, 2010).
33. A. Cafarelli, P. Miloro, A. Verbeni, M. Carbone, and A. Menciassi, "Speed of sound in rubber-based materials for ultrasonic phantoms," *Journal of ultrasound* **19**(4), 251–256 (2016).
34. L. Warnes, "Some acoustical properties of certain polyurethane elastomers," *Ultrasonics* **27**(2), 97–100 (1989).
35. P. H. Mott, C. M. Roland, and R. D. Corsaro, "Acoustic and dynamic mechanical properties of a polyurethane rubber," *J. Acoust. Soc. Am.* **111**(4), 1782–1790 (2002).
36. M. D. van Erk, A. J. Dam-Vervloet, F.-A. de Boer, M. F. Boomsma, H. v. Straaten, and N. Bosschaart, "How skin anatomy influences transcutaneous bilirubin determinations: an in vitro evaluation," *Pediatr. Res.* **86**(4), 471–477 (2019).
37. A. J. Dam-Vervloet, M. D. van Erk, N. Doorn, S. G. Lip, N. A. Timmermans, L. Vanwinsen, F.-A. de Boer, H. L. van Straaten, and N. Bosschaart, "Inter-device reproducibility of transcutaneous bilirubin meters," *Pediatr. Res.* **89**(4), 770–775 (2021).
38. "Optical absorption of melanin," <https://omlc.org/spectra/melanin/>. Accessed: 2023-06-29.
39. M. C. Mack, N. K. Tierney, E. Ruvalo, G. N. Stamatas, K. M. Martin, and N. Kollias, "Development of solar UVR-related pigmentation begins as early as the first summer of life," *J. Invest. Dermatol.* **130**(9), 2335–2338 (2010).
40. N. Bosschaart, R. Mentink, J. H. Kok, T. G. Van Leeuwen, and M. C. Aalders, "Optical properties of neonatal skin measured in vivo as a function of age and skin pigmentation," *J. Biomed. Opt.* **16**(9), 097003 (2011).
41. B. E. Treeby and B. T. Cox, "k-wave: Matlab toolbox for the simulation and reconstruction of photoacoustic wave fields," *J. Biomed. Opt.* **15**(2), 021314 (2010).
42. W. V. Sorin and D. Gray, "Simultaneous thickness and group index measurement using optical low-coherence reflectometry," *IEEE Photonics Technol. Lett.* **4**(1), 105–107 (1992).
43. C. Cuartas-Vélez, C. Veenstra, S. Kruitwagen, W. Petersen, and N. Bosschaart, "Optical density based quantification of total haemoglobin concentrations with spectroscopic optical coherence tomography," *Sci. Rep.* **11**(1), 8680 (2021).

44. C. Veenstra, S. Kruitwagen, D. Groener, W. Petersen, W. Steenbergen, and N. Bosschaart, "Quantification of total haemoglobin concentrations in human whole blood by spectroscopic visible-light optical coherence tomography," *Sci. Rep.* **9**(1), 15115 (2019).
45. C. Veenstra, W. Petersen, I. M. Vellekoop, W. Steenbergen, and N. Bosschaart, "Spatially confined quantification of bilirubin concentrations by spectroscopic visible-light optical coherence tomography," *Biomed. Opt. Express* **9**(8), 3581 (2018).
46. D. Liu and J. Yu, "Otsu method and k-means," *IEEE International Conference on Hybrid Intelligent Systems* **1**, 344 (2009).
47. R. Bulsink, M. Kuniyil Ajith Singh, M. Xavierselvan, S. Mallidi, W. Steenbergen, and K. J. Francis, "Oxygen saturation imaging using led-based photoacoustic system," *Sensors* **21**(1), 283 (2021).
48. K. J. Francis, R. Booiijink, R. Bansal, and W. Steenbergen, "Tomographic ultrasound and led-based photoacoustic system for preclinical imaging," *Sensors* **20**(10), 2793 (2020).
49. M. Jaeger, S. Schüpbach, A. Gertsch, M. Kitz, and M. Frenz, "Fourier reconstruction in optoacoustic imaging using truncated regularized inverse k-space interpolation," *Inverse Problems* **23**(6), S51–S63 (2007).
50. Z. Wang, A. C. Bovik, H. R. Sheikh, and E. P. Simoncelli, "Image quality assessment: from error visibility to structural similarity," *IEEE Transactions on Image Processing* **13**(4), 600–612 (2004).
51. T. Collier, D. Arifler, A. Malpica, M. Follen, and R. Richards-Kortum, "Determination of epithelial tissue scattering coefficient using confocal microscopy," *IEEE J. Sel. Top. Quantum Electron.* **9**(2), 307–313 (2003).
52. T. Lister, P. A. Wright, and P. H. Chappell, "Optical properties of human skin," *J. Biomed. Opt.* **17**(9), 0909011 (2012).
53. P. Kubelka and F. Munk, "An article on optics of paint layers," *Z. Tech. Phys* **12**, 259 (1931).
54. S. A. Prahl, M. J. van Gemert, and A. J. Welch, "Determining the optical properties of turbid media by using the adding–doubling method," *Appl. Opt.* **32**(4), 559–568 (1993).
55. J. W. Pickering, S. A. Prahl, N. Van Wieringen, J. F. Beek, H. J. Sterenborg, and M. J. Van Gemert, "Double-integrating-sphere system for measuring the optical properties of tissue," *Appl. Opt.* **32**(4), 399 (1993).